An efficient computational framework for hydrofoil characterisation and tidal turbine design

Shane C. Heavey [1,3,4], Sean B. Leen[1,3,4], Patrick J. McGarry[2,3,4*]
[1]Mechanical Engineering, NUI Galway, Ireland
[2]Biomedical Engineering, NUI Galway, Ireland
[3]Ryan Institute, NUI Galway, Ireland
[4]Centre for Marine and Renewable Energy Ireland (MaREI), Galway Ireland
*Corresponding author: patrick.mcgarry@nuigalway.ie

Abstract

Blade element momentum (BEM) modelling offers a computationally inexpensive means of analysing turbine performance. Lift and drag coefficient data-sets specific to the operating conditions of the turbine must be input into a BEM model. However, such data is not typically available over the wide range of Reynolds number (*Re*) and angle of attack (α) encountered by vertical axis turbines. This paper presents a computational fluid dynamics (CFD) approach, based on transitional flow turbulence modelling, to determine lift and drag coefficients for a symmetric hydrofoil. Results are validated against published experimental data for a wide range of α and *Re*. It is demonstrated that BEM models provide improved predictions of vertical axis turbine performance when CFD generated lift and drag coefficients are used as input, rather than coefficients generated by the widely used panel-method. The combined CFD-based BEM methodology achieves a similar level of accuracy to a full CFD turbine model while providing a significant reduction in computational cost. The modelling approach and hydrofoil data-set developed in this study can be directly utilised for the design and optimisation of next-generation non-straight bladed vertical axis turbine designs which operate over a wide range of α and *Re*.

***Keywords*—** CFD, lift & drag coefficient, angle of attack, Reynolds number, BEM

1. Introduction

In a continually developing global energy market there is an ever-increasing need to investigate alternative options for sustainable and predictable electricity generation. Tidal energy provides significant advantages over competing resources, including predictability and repeatability. A recent resource assessment estimated that there is an annual mean tidal resource of 4 TJ available in the Irish Sea based on 1st generation tidal turbines which require a spring tide velocity greater than 2.5 m/s (Lewis et al., 2015).

Research is currently on-going into the development of tidal stream generators with much of the focus being placed on large-scale horizontal axis tidal turbines (HATTs) (Goundar and Ahmed, 2013). Vertical axis tidal turbines (VATTs) are not as commonly explored commercially as HATTs, as previous results have shown that these turbines generally tend to have lower power efficiencies at larger scales (Roberts et al., 2016). However, VATTs have gained renewed interest due to the realisation of their enhanced performance for small-scale application (Battisti et al., 2016; Hill et al., 2009; Svorcan et al., 2013). Several novel turbine designs have recently been proposed (Preen and Bull, 2015; Shires, 2013). Due to their geometry, VATTs can be designed to span a wider area than HATTs in a relatively shallow flow field, resulting in increased resource access. Additionally, VATTs are omnidirectional and do not require a pitching or yawing mechanism to adjust the turbine blades, resulting in fewer machine components, simpler operating systems and lower maintenance costs.

Blade element momentum (BEM) modelling offers a computationally inexpensive method for preliminary analysis of a turbine design. Hydrofoil lift and drag coefficients, C_L and C_D, are the key inputs required for a BEM model. These coefficients must be specified for the turbine operating range of Reynolds number, *Re*, and angle of attack, α.

Optimum hydrodynamic conditions avoid the occurrence of stall. This can be achieved by restricting the variation in α to a narrow range. This is readily achieved for HATTs by designing the blade pitch so as to minimise the range of α, even when operating outside of optimum conditions. However, for VATTs, as the azimuthal angle varies between 0° and 360°, a wide range of α is encountered, especially at low tip-speed ratios (*TSR*). *TSR* is the ratio of the radial velocity of the turbine blade to the incoming freestream velocity. As shown in Fig. 1, straight bladed VATTs operating at optimum power performance (*TSR* = 4) typically experience α values between -12° and 12°. At lower *TSRs* a higher range is encountered,

increasing the probability that a blade will enter the stall region for significant periods. A large variation in *Re* is also evident in Fig. 1.

C_L and C_D data are not generally available for such a wide range of α and *Re*, even for standard aerofoil/hydrofoil designs. As an example, in the case of the commonly used NACA 0015 profile experimental characterisation is limited to a small range of α (Jacobs and Sherman, 1937), or a small range of *Re* (Sheldahl and Klimas, 1981).

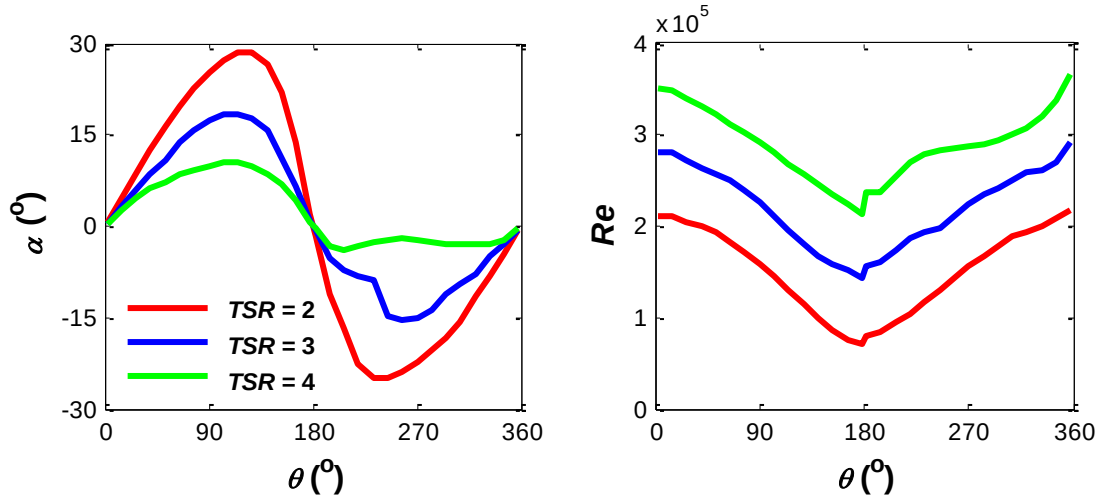

Fig. 1. Variation of α and *Re* with azimuthal angle for various operating *TSR* for a straight-bladed VATT. Results taken from previously developed BEM code

Recent innovations include the development of curved and spiralling blade geometries (Cheng et al., 2017; Talukdar et al., 2017; Walsh et al., 2015), in particular for vertical axis and cross-flow turbines. One such innovative turbine design (McGuire, 2014) (Fig. 2) is considered in this paper. Potential advantages of this novel blade geometry include increased power efficiency over existing technologies and a reduction in the magnitude of cyclic loads on vertical-axis tidal turbines (Heavey et al., 2018). However, complex spiral-type blade geometries encounter an increased range of *Re* and α during operation compared to equivalent straight blade turbine designs. In the case of the turbine prototype shown in Fig. 2 the value of α at a blade section depends on the axial coordinate in addition to the azimuthal angle.

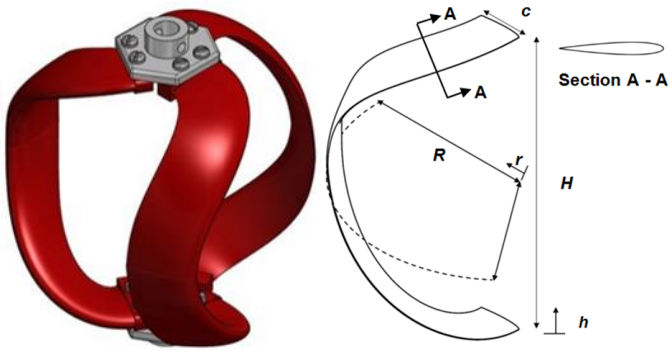

Fig. 2. Schematic of initial *Bri Toinne Teoranta* turbine and blade design (Patent number US 8690541, McGuire, 2014) where *R* is the maximum blade radius, *H* is the total blade height and *c* is the blade chord length.

Even at the optimal operating conditions, as shown in Fig. 3, a wide range of α is encountered and *Re* can vary by several orders of magnitude along a blade. In order to reliably design and optimise next-generation spiral bladed turbines using the BEM approach, C_L and C_D data must be determined for such an extensive range of operating conditions.

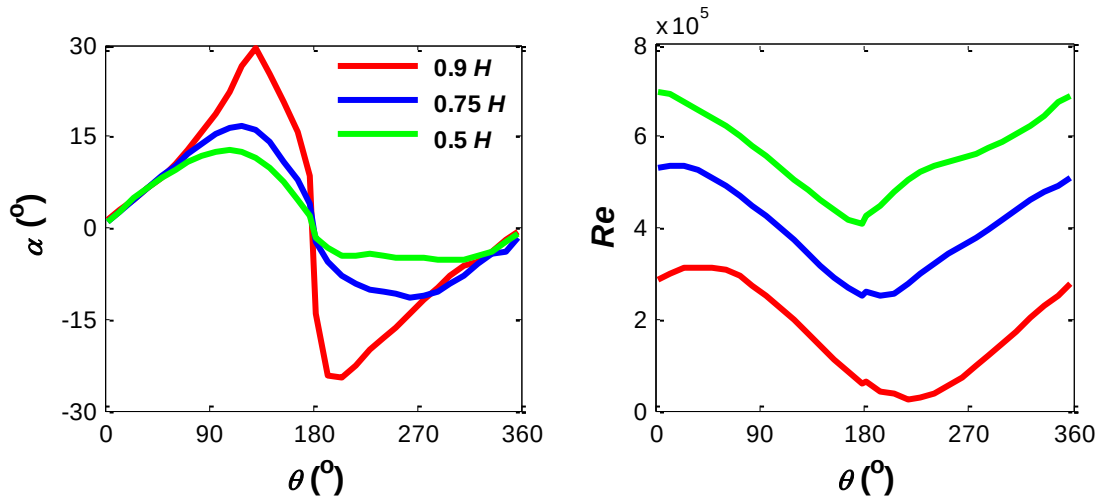

Fig. 3. Variation of α and Re with turbine height for novel turbine design (TSR = 4). Results taken from previously developed BEM code.

The panel method (Eppler, 1978) offers a means of determining of C_L and C_D for high values of Re ($Re > 5 \times 10^5$). A study presents panel method (PROFIL) derived C_L and C_D data-sets for a range of Re values from 10^4 to 10^7 for seven symmetrical NACA aerofoil profiles (Sheldahl and Klimas, 1981). However, the panel method is not accurate for conditions that result in flow separation, i.e. it should not be used for high values of α and low values of Re. Fig. 4 presents a comparison of panel method predictions to experimentally measured C_L for $Re = 8.4\times 10^4$. Clearly, the method does not accurately predict the stall region, which occurs for $\alpha > 8^o$. Fig. 3 illustrates that such low values of Re and high values of α are relevant to the design of next-generation turbines. Therefore an accurate method of determining C_L and C_D must be established.

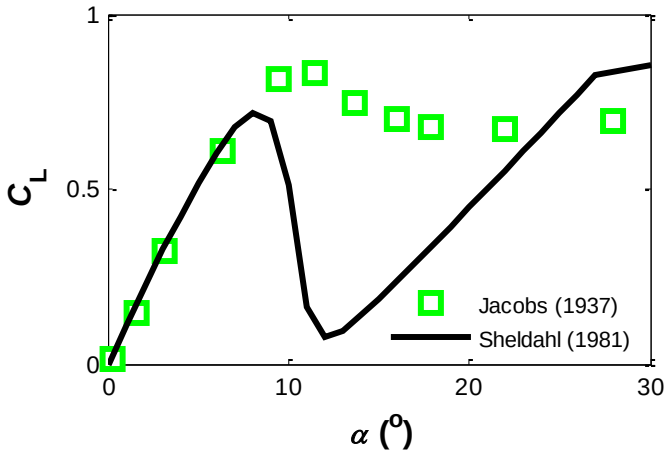

Fig. 4. Comparison between PROFIL (Sheldahl and Klimas, 1981) and experimental results (Jacobs and Sherman, 1937) for NACA0015 ($Re = 8.4 \times 10^4$).

Due to recent advances in computing power CFD analysis of hydrofoils, under a wide range of test conditions with a sufficiently high spatial and temporal discretisation, and an appropriate turbulence model presents an alternative methodology to determine C_L and C_D hydrofoil data-sets for a wide range of flow conditions. Such information can potentially provide accurate input for BEM analysis of next-generation VATTs with spiral blade designs so that initial design parametric studies can be performed in an efficient manner.

Full turbine CFD analyses have been studied previously, especially in the case of two-dimensional models for straight-bladed wind-based vertical-axis turbine (Almohammadi et al., 2013; Maître et al., 2013; McNaughton et al., 2014). While these methods have been found to be accurate, they are not commonly implemented as a design optimisation tool due to the enormous computational resources required.

The aim of this study is to:

- *Establish a CFD methodology that provides accurate and computationally efficient values of C_L and C_D for a hydrofoil geometry under a wide range of flow conditions.*
- *Demonstrate the improved accuracy of the BEM approach to VATT analysis when CFD derived C_L and C_D data-sets are used as model input.*
- *Compare the computational resource requirement and accuracy of a full CFD study of a VATT to the CFD-based BEM methodology developed in this paper.*

2. Hydrofoil Geometry

The NACA0015 is a commonly studied NACA series profile. The design is frequently used for VATs and is the hydrofoil chosen for the novel turbine design shown in Fig. 2. This blade profile is a symmetrical profile. The profile has no camber (as indicated by "00"), and the profile has a maximum thickness of 15% of the overall chord length (as indicated by "15") which occurs at 40% of the distance along the chord line from the leading edge. A hydrofoil of a chord length of 1 m was chosen for this study.

Hydrofoils of varying shapes have different characteristics for different operating conditions. To analyse the performance of hydrofoils it is necessary to compare their non-dimensional C_L and C_D, defined in equations (1) and (2).

$$C_L = \frac{2F_L}{\rho A {U_{i,H}}^2} \tag{1}$$

$$C_D = \frac{2F_D}{\rho A {U_{i,H}}^2} \tag{2}$$

where ρ is the fluid density, $U_{i,H}$ is the hydrofoil inlet velocity and A is the area of the blade (chord × span).

The total force component along the specified force vector $\vec{a}$ on the hydrofoil is computed by summing the dot product of the pressure and viscous forces on each face of the hydrofoil with the specified force vector (ANSYS, 2013). The terms in this summation represent the pressure and viscous force components in the direction of the vector $\vec{a}$:

$$F_a = \vec{a}.\vec{F_p} + \vec{a}.\vec{F_v} \tag{3}$$

where $\vec{a}$ is the specified force vector, $\vec{F_p}$ is the pressure force vector and $\vec{F_v}$ is the viscous force vector. The pressure force vector is calculated as:

$$\vec{F_p} = \sum_{i=1}^{n} (p(i) - p_{ref}) A(i) \hat{n} \tag{4}$$

where n is the number of faces, p is the pressure, p_{ref} is a reference pressure, A is the area of the face and $\hat{n}$ is the unit normal to the face. The viscous force vector is calculated as:

$$\vec{F_v} = \sum_{i=1}^{n} \mu(i) \frac{\partial u(i)}{\partial y} A(i) \tag{5}$$

Where $\mu(i)$ is the local dynamic viscosity, u is the flow velocity parallel to the face and y is the distance to the wall. F_a is resolved into components perpendicular and parallel to the incoming flow to determine the lift and drag force (F_L and F_D) respectively.

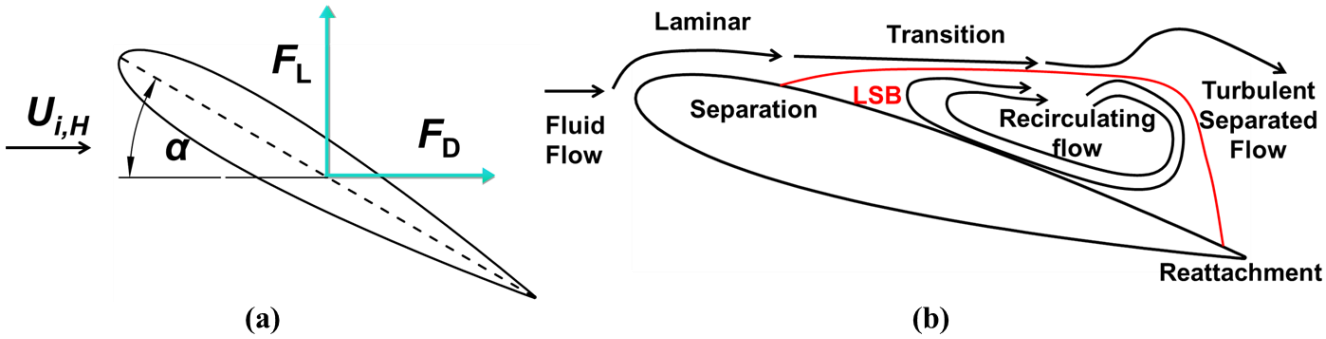

Fig. 5. (a) Lift and drag force acting on a hydrofoil; (b) Flow structures around a hydrofoil under stall conditions showing the laminar separation bubble (LSB), described in detail in Section 3.

3. CFD Model Development

Common numerical modelling methods within CFD are direct numerical simulation (DNS), large eddy simulations (LES), detached eddy simulation (DES) and Reynolds-averaged Navier-Stokes (RANS) modelling. DNS involves solving all scales of flow and is the most accurate modelling technique. DNS has previously been utilised to predict the flow around NACA profiles. However, due to the enormous computational expense, this study has been limited to analysis of single α value at a single *Re* (Shan et al., 2005). LES involves solving the largest scale motions of flow and modelling the small-scale motions. LES has proven to be very accurate in predicting lift and drag forces (Li et al., 2013). However, due to the three-dimensionality requirement of LES models, it is too computationally intensive and is not a practical approach for determination of C_L and C_D for a large range of α and *Re*. DES is a modification of a RANS model in which the model switches to a sub-grid scale formulation in regions where the mesh is fine enough for LES calculations. Regions near solid boundaries and where the turbulent length scale is less than the maximum grid dimension are assigned the RANS mode of solution. For RANS modelling all the unsteadiness in the turbulent flow is averaged. Due to the complexity of turbulence, it is unlikely that any single RANS turbulence model is fully capable of representing all turbulent flows. However, it has proven to be an accurate means of determining the average forces on a large scale body (Stergiannis et al., 2016). Owing to the high computational cost of DNS, LES and DES, this study implements RANS turbulence modelling.

Previous CFD RANS approaches to determining C_L and C_D data for aerofoils have been limited to single Reynolds number values and/or low pre-stall angles of attack due to use of Spallart-Allamaras, k-ε, or k-ω turbulence models (Azeez and Paul, 2014; Dash, 2016; Douvi et al., 2012; Sagmo et al., 2016; Şahin and Acir, 2015; Wang et al., 2010). Previously studied turbulence models i.e. Spallart-Allamaras, k-ε, and k-ω, assume that the entirety of the flow in the fluid domain is turbulent. While these approaches are very computationally efficient, they fail to capture flow separation, the laminar separation bubble (LSB), and flow reattachment, all shown in Fig. 5 (b). All of these phenomena are strongly influenced by the laminar to turbulent flow transition in the hydrofoil boundary layer and contribute significantly to the prediction of lift and drag forces in the critical stall region. The shear stress transport transition (SST-T) model (Menter et al., 2006) has been shown to predict the laminar to turbulent transition and flow separation (Langtry et al., 2006). It, therefore, provides an appropriate approach for the analysis of hydrofoils at high angles of attack. The SST-T model has previously been implemented for symmetric and non-symmetric aerofoil analyses (Counsil and Goni Boulama, 2013, 2012; Genç, 2010). In all cases, the superior ability of the SST-T model to predict the flow around the aerofoil is presented. However, these studies have only simulated a limited range of values of *Re* and of α. As shown in Section 1, BEM analysis of vertical axis turbines requires data for a very large range of *Re* and of α, hence the requirement for a comprehensive study to assess the capability of the SST-T model to predict C_L and C_D over this desired range.

SST-T Model Development

The SST-T is based on the SST k-ω turbulence model (Menter, 1994), with two additional equations. The SST k-ω model switches between the standard k-ε model in the far field, free-stream region and the k-ω model at the wall surfaces, with a y+ value of less than 1 required for a well-defined boundary layer. The y+ value is a non-dimensional wall distance which indicates how fine or coarse a mesh is along a wall surface. The benefit of the SST k-ω model is that neither the k-ε nor k-ω model deals with the entire flow field particularly well. The k-ε model predicts the flow in the free stream very well but it does not accurately predict high flow separation or reverse flow situations from the wall, both of which are possible

situations for hydrofoils, especially at high values of α. Contrastingly, the k-ω model performs well for near wall conditions but encounters difficulties with defining inlet free-stream turbulence properties.

The SST k-ω model is a fully turbulent model which assumes that all the fluid in the model domain in turbulent. This, however, may not be the case so the SST-T model incorporates two additional equations for the intermittency (γ) and the transitional momentum thickness Reynolds number ($Re_{\theta t}$). γ is used to determine whether the SST-T model should be active. When γ is zero, the production of turbulent kinetic energy is suppressed and the flow is effectively laminar. When γ is equal to one, the SST-T model is fully active and the flow is assumed to be fully turbulent. $Re_{\theta t}$ controls the transition criterion between laminar and turbulent flow. The critical Reynolds number, $Re_{\theta c}$, occurs where intermittency begins to increase in the boundary layer. It occurs upstream of the transition Reynolds number, $Re_{\theta t}$, as turbulence must first build up to appreciable levels in the boundary layer before any change in the laminar profile can occur. As a result, $Re_{\theta c}$ is the location where turbulence starts to grow and $Re_{\theta t}$ is the location where the velocity profile starts to deviate from a purely laminar profile. The equations associated with this turbulence model and a more in-depth analysis of this model can be found in (Menter et al., 2006; Langtry et al., 2006).

Mesh definition is of primary importance for this approach when defining a RANS simulation. Key parameters in determining the mesh refinement include the non-dimensional distance to the first cell from a wall (y+ value), the growth rate at the walls, the number of elements in the boundary layer, the number of nodes on the surface of the hydrofoil and the overall size of the domain.

To fully capture the flow effects around the hydrofoil, transient simulations are required. Flow separation and reattachment are time-dependent so it is necessary to carry out parametric studies to identify the required time step and the required simulation time to achieve a converged solution.

3-1. Hydrofoil model

The density of water is set at 998.2 kg m^{-3}, and the viscosity, μ, is set at 1.003×10^{-3} kg m^{-1} s^{-1}. *Re* is changed for each case by varying the incoming hydrofoil inlet velocities, $U_{i,H}$. It is calculated as follows:

$$Re = \frac{\rho U_{i,H} c}{\mu} \tag{6}$$

where c is the blade chord length.

The two-dimensional computational C-grid is generated using ICEM within ANSYS Workbench. A scripting code is developed to replicate meshing parameters for each α value to ensure the same mesh characteristics are defined in each case. A blocking framework is implemented to represent the topology of the model. This blocking framework is associated with the model geometry. A structured quadrilateral grid is generated within each block, shown in Fig. 6. Three blocks are generated around the hydrofoil wall to ensure adequate refinement close to the hydrofoil wall. A key requirement of the SST-T model is a $y^+ < 1$. The initial first layer height, y, is calculated using equation (7). Fifty inflation layers are used with a growth rate of 1.15 implemented for all grid generations.

$$y = \frac{y^+ \upsilon}{V_*} \tag{7}$$

where V_*, the friction velocity is defined as,

$$V_* = \frac{\tau_w}{\rho} \tag{8}$$

A systematic approach is adopted to carry out a detailed mesh refinement study to ensure an accurate solution is achieved detailed in Section 4-1.1. Five meshes with different numbers of elements are generated with the focus being placed on refining the critical boundary layer around the hydrofoil surface.

The inlet velocity applied to the domain varied for each *Re*. A turbulent intensity of 0.2% and turbulent viscosity ratio of 2 is applied at the inlet also. The hydrofoil surface is defined as a no-slip wall. The outlet is defined as a pressure outlet with 0 Pa gauge pressure. A symmetry boundary condition is applied to the top and bottom surface of the domain.

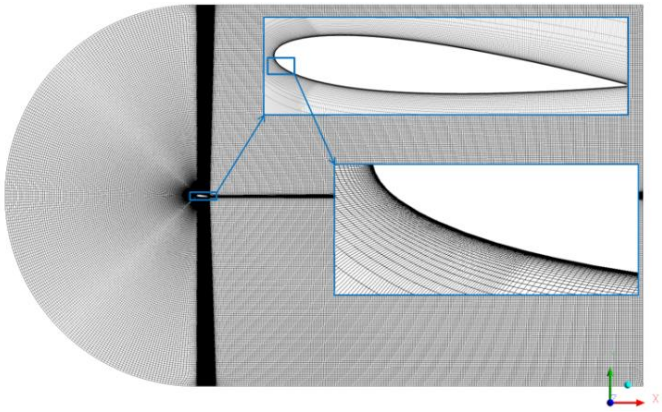

Fig. 6. Structured mesh around NACA0015 showing detailed inflation around hydrofoil in the critical boundary layer region ($\alpha = 10^o$).

Parametric studies are performed to determine the necessary domain size for a converged solution. This study reveals that to ensure a fully developed wake, the length of the domain is set at 40 m and width at 30 m, both based on a hydrofoil chord length of 1 m.

The models are solved using the finite volume method with the CFD RANS based code within ANSYS FLUENT. As the flow regime in the stall and post-stall regime is unsteady, a second order implicit transient simulation formulation is implemented. The SIMPLE algorithm is used to solve the coupling between the velocity components and pressure in momentum equations. A transient pressure based model is set up with a Green-Gauss cell-based method applied for the pressure gradient. Second order upwind discretisation methods are applied to the momentum, turbulent kinetic energy, specific dissipating rate, intermittency and transitional Reynolds number equations. Second order algorithms result in more accurate predictions as they reduce interpolation errors and false numerical diffusion in comparison to first order algorithms. The convergence criterion is set as a target value of 10^{-6} for all residuals. Calculations are run using 24 processors and the total runtime of the simulation was dependant on the *Re* and α. Low values of α require 1-hour run-time to reach a converged solution. Higher α value simulations require between 8 and 24 hours run-time to reach a converged solution, with high values of α at low *Re* requiring the longest run-times. Further details on the temporal discretisation studies are listed in Section 4-1.1. It should be noted that for angles of attack in the stall and post-stall region, a constant steady-state lift or drag coefficient is not achieved due to the unsteady nature of the flow under these conditions, i.e. vortex shedding. This is discussed in detail in Section 4-2.

3-2. Full turbine model

In order to assess the accuracy of a BEM turbine analysis with CFD based hydrofoil C_L and C_D input, results are compared to a full CFD analysis of a standard straight-bladed vertical axis turbine design. The turbine parameters are listed in Table 1.

Table 1
Straight-bladed vertical axis turbine geometrical parameters.

Parameter	Value
Length (L)	3 m
Diameter (D)	2.5 m
Chord (c)	0.4 m
Number of blades	3
Blade profile	NACA0015

Following from the hydrofoil simulations in Section 3-1, the full CFD model of the turbine also uses the SST-T turbulence model. Model boundary conditions and domain dimensions are shown in Fig. 7. The boundary conditions simulate free stream conditions ensuring the turbine performance is not affected by blockage effects and the wake is allowed to fully develop. Free-stream conditions were simulated for the CFD calculations to reduce the mesh size requirements. The three

turbine blade surfaces are set as non-slip walls. Two cell zones are defined to develop a moving reference frame model, also known as 'the frozen rotor approach', to simulate the rotating turbine blades. An interface, shown in Fig. 7, is defined between the moving and stationary cell zones. The steady state flow field solution from the moving reference frame simulation is used as the initial solution for the transient sliding mesh calculation, thus reducing the overall time to achieve a converged solution. First order upwind discretisation schemes are applied for the momentum, turbulent kinetic energy, specific dissipating rate, intermittency and the transitional Reynolds number for the first 8 turbine rotations before switching to second order discretisation schemes for the remaining rotations to increase the solution accuracy.

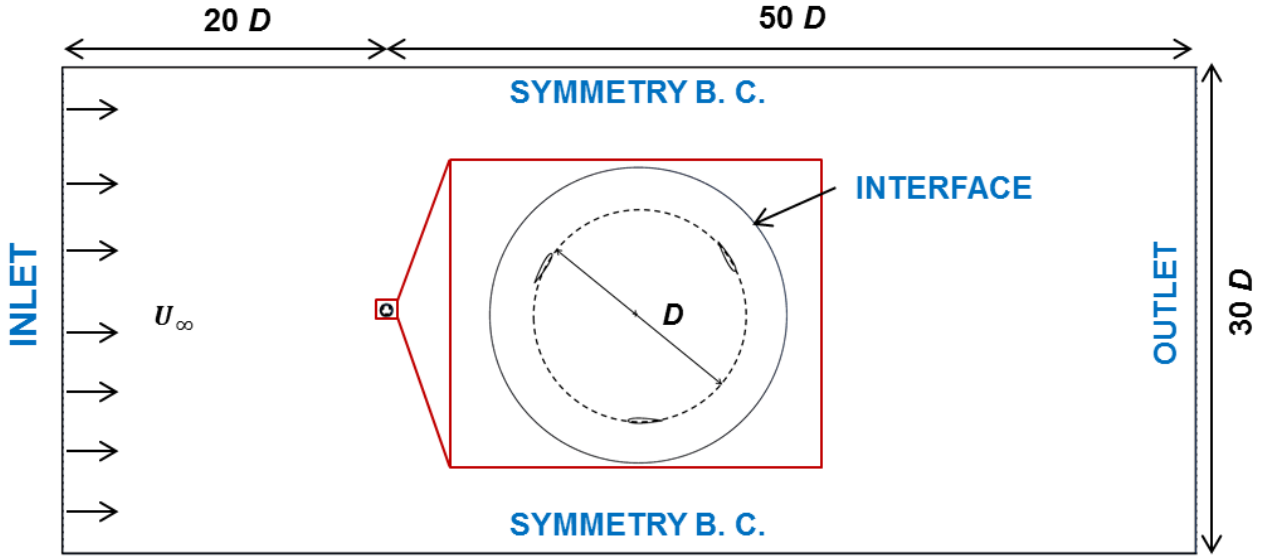

Fig. 7. Computational domain for 2D simulations of straight bladed vertical axis turbine of diameter D. Boundary conditions and rotating cell zone indicated.

The CFD mesh is systematically refined to identify the optimum spatial discretisation with the focus placed on the critical region around the blade surfaces. Similar to the hydrofoil study, the initial first layer height, *y*, around the blade surfaces is defined by equation 7 to ensure a y^+ value < 1. Similar mesh sizing is applied on either side of the stationary and rotating interface to ensure a consistent mesh size is achieved in this region. Computed results from a spatial discretisation study are presented in Section 4-1.2. Figure 8 shows a CFD turbine mesh containing 861660 elements, highlighting mesh refinement at key regions including inflation layers at hydrofoil walls.

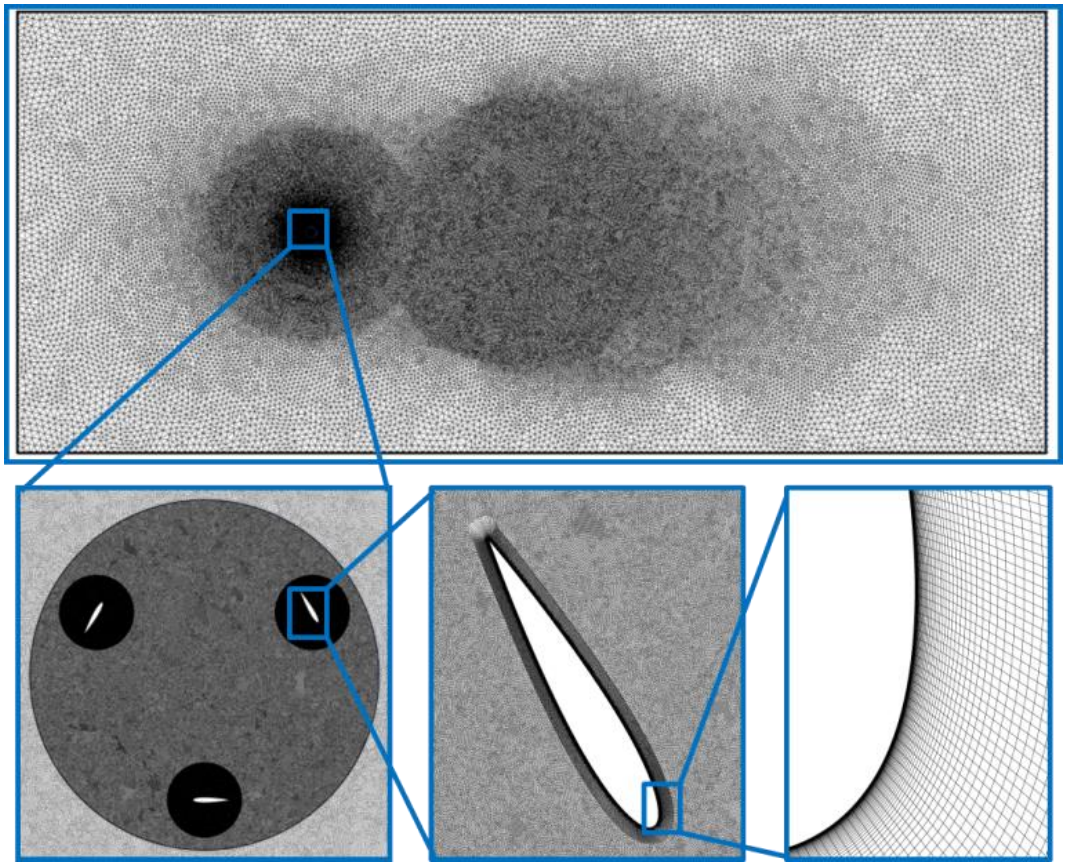

Fig. 8. Image of Mesh C (see Table 2) showing refinement at key regions including inflation layers at hydrofoil walls.

Simulations are carried out for *TSR*s varying from 0.5 to 2.5. The rotational velocity, ω_{rot}, is applied to the three blades in accordance with equation 9, where R is the turbine radius and U_∞ is the fluid freestream velocity.

$$\omega_{\text{rot}} = \frac{U_\infty TSR}{R} \tag{9}$$

The instantaneous torque coefficient, C_{Q}, is determined for each time step based on the following equation:

$$C_{\text{Q}} = \frac{Q_{\text{i}}}{0.5\rho A {U_\infty}^2 R} \tag{10}$$

where Q_{i} is the instantaneous torque, U_∞ is the freestream velocity and A is the turbine frontal area. An averaged torque coefficient for each rotation, $\bar{C}_{\text{Q}}$, is calculated by:

$$\bar{C}_{\text{Q}} = \frac{1}{2\pi}\int_0^{2\pi} C_{\text{Q}}\, d\theta \tag{11}$$

Simulations are run until a converged $\bar{C}_{\text{Q}}$ was achieved. The solution is deemed to have achieved the convergence criterion when the variation of $\bar{C}_{\text{Q}}$ between two subsequent rotations is less than 0.5 %. The average power coefficient, C_{Power}, for the given *TSR*, is calculated as follows:

$$C_{\text{Power}} = \bar{C}_{\text{Q}} TSR \tag{12}$$

4. Results

The Results section is structured as follows: (4-1) Preliminary spatial and temporal discretisation parametric studies are first performed to ensured converged CFD solutions are achieved; (4-2) Validated discretisation parameters are then used to generate C_L and C_D for three different Reynolds: 8.4 x 10^4, 5 x 10^5 and 1.27 x 10^6, for values of α up to 30°. Results for these *Re* values are compared with previously published panel method and experimental results. CFD results for the pressure coefficient variation along the hydrofoil's upper and lower surfaces are also compared to experimental results to provide further model validation; (4-3) this data-set is implemented in a BEM code and results are compared with panel method based BEM code results and full CFD VAT studies with all results validated against experimental data; (4-4) finally, the CFD dataset is implemented for the novel turbine geometry.

4-1. Discretisation studies

Fully discretised models in both space and time are developed for both the single hydrofoil and full turbine CFD simulations. This ensures a mesh and time increment independent result is achieved. This provides confidence in the models when validating against physical test data.

4-1.1. Hydrofoil model

Spatial Discretisation

Various simulations are carried out in order to determine the required level of mesh refinement to achieve converged solutions for the C_L and C_D. Richardson extrapolation (Roache, 1997) is used to calculate the exact solution based on the convergence and refinement ratio determined using a series of five increasingly refined meshes. Before applying Richardson extrapolation it is necessary to determine the apparent convergence condition based on the R^*, defined as:

$$R^* = \frac{C_{L,2} - C_{L,1}}{C_{L,3} - C_{L,2}} \tag{13}$$

$R^*>1$ Monotonic divergence
$1 > R^* > 0$ Monotonic convergence
$0 > R^* > -1$ Oscillatory Convergence
$R^* < -1$ Oscillatory divergence

Richardson extrapolation may only be used when the apparent convergence condition is monotonic. C_L and C_D are determined for each of the five meshes for an α value of 10° and *Re* of 1×10^6. A constant mesh refinement ratio, *r*, defined in equation (14), of 1.67 was applied.

$$r = \left(\frac{N_{\text{fine}}}{N_{\text{coarse}}}\right)^{\frac{1}{2}} \tag{14}$$

where N_{fine} is the number of elements in the fine mesh and N_{coarse} is the number of elements in the coarse mesh. The order of convergence, *p*, is defined as:

$$p = \frac{\ln\left(\frac{C_{L,2} - C_{L,1}}{C_{L,3} - C_{L,2}}\right)}{\ln(r)} \tag{15}$$

Table 2 presents the C_L and C_D for the five meshes. The final Richardson's extrapolation values are also displayed. The Richardson's extrapolation value for the C_L was calculated as follows:

$$C_L = C_{L,1} + \frac{C_{L,1} - C_{L,2}}{r^p - 1} + HOT \tag{16}$$

where *HOT* are the higher order terms. The same formula is used to calculate the Richardson's extrapolation value for C_D.

Table 2

C_L and C_D results for a series of five increasingly refined meshes for an angle of attack of 10° and Re of 1×10^6.

Mesh	Total Elements	C_L	C_D	% C_L	% C_D
M1	9000	0.891	0.0271	10.2	-35.9
M2	25100	0.981	0.0221	1.1	-10.8
M3	70300	0.991	0.0205	0.13	-3.0
M4	195220	0.992	0.0201	0.06	-0.6
M5	544470	0.992	0.0199	0.02	-0.03
Richardson's extrapolation value		0.992	0.02		

From the spatial discretisation study, it can be concluded that model predictions using M4 and M5 are very similar to each other. Fig. 9 shows C_L variation with the normalised mesh size for the five meshes and the final Richardson extrapolation value. M4 results for C_L and C_D are within 1% of the final Richardson's extrapolation value. Spatial discretisation studies were also performed for $\alpha = 5^o$ and $\alpha = 25^o$ at two Reynolds number $Re = 1 \times 10^5$ and $Re = 1 \times 10^6$. The same mesh, M4, provided the desired criteria for convergence for each simulation. Based on this analysis the M4 mesh is used for all subsequent simulations.

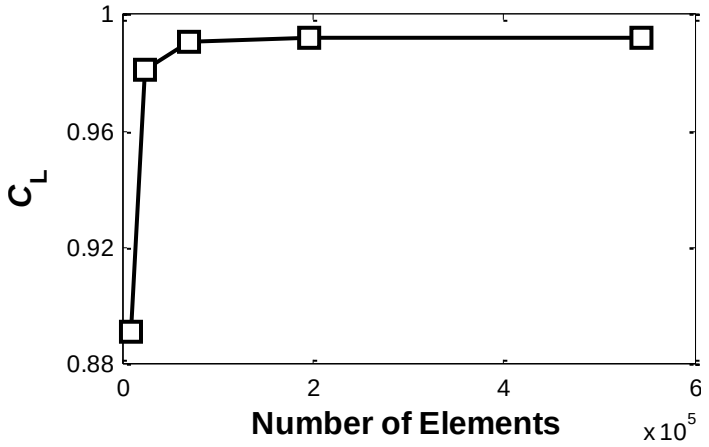

Fig. 9. Mesh convergence study results for $\alpha = 10^o$ and $Re = 1\times10^6$.

Temporal Discretisation

Transient simulations are required for all SST-T calculations as this model predicts the transition from laminar to turbulent which is highly time-dependent. A number of time-steps (Δt) have been investigated ($\Delta t = 0.1$ s, $\Delta t = 0.05$ s, $\Delta t = 0.01$ s, $\Delta t = 0.005$ s, $\Delta t = 0.0005$ s) to determine the required step size to compute converged solutions for C_L and C_D. This parametric analysis is critical due to the highly transient nature of the flow, particularly at high α. Computed values of C_L and C_D for a range of time steps for three α values, 5°, 15° and 25°, are shown in Tables 3-5. Clearly, different α values require different time steps due to the unsteady nature of the flow under stall conditions. Based on this parametric study the following temporal discretisation is used in subsequent simulations: $\Delta t = 0.05$ s for $\alpha \leq 10^o$; $\Delta t = 0.01$ s for $10^o < \alpha \leq 20^o$; $\Delta t = 0.005$ s for $20^o < \alpha \leq 30^o$. It should also be noted that for increasing α and decreasing Re the simulations needed a longer runtime to reach a converged solution, this is due to the highly unsteady nature of the flow at these circumstances.

Table 3
C_L and C_D computed for a range of Δt for angle of attack of 5°.

	$Re = 1\times 10^5$		$Re = 1\times 10^6$	
Δt (s)	C_L	C_D	C_L	C_D
0.1	0.611	0.0218	0.561	0.0099

0.05	0.609	0.0217	0.535	0.0092
0.01	0.609	0.0217	0.535	0.0091
0.005	-	-	0.535	0.0091
0.0005	-	-	-	-

Table 4
C_L and C_D computed for a range of Δt for angle of attack of 15°.

	$Re = 1\times 10^5$		$Re = 1\times 10^6$	
Δt (s)	C_L	C_D	C_L	C_D
0.1	0.669	0.211	1.331	0.0395
0.05	0.675	0.213	1.330	0.0396
0.01	0.677	0.214	1.326	0.0393
0.005	0.677	0.214	1.324	0.0393
0.0005	-	-	1.324	0.0393

Table 5
C_L and C_D computed for a range of Δt for angle of attack of 25°.

	$Re = 1\times 10^5$		$Re = 1\times 10^6$	
Δt (s)	C_L	C_D	C_L	C_D
0.1	0.994	0.523	1.223	0.652
0.05	0.920	0.495	1.064	0.563
0.01	0.909	0.490	0.930	0.495
0.005	0.905	0.489	0.921	0.490
0.0005	0.905	0.489	0.919	0.489

4-1.2. Full turbine model

Spatial discretisation

Four increasingly refined meshes are analysed (details provided in Table 6). The number of nodes on blade surfaces and the total number of elements in the inflation layers are consistent with values used in the hydrofoil spatial discretisation study presented in Section 4-1.1 above.

Table 6
CFD mesh parameters for spatial discretisation study of vertical axis turbine.

Mesh	No. Elements Rotating	No. Elements Stationary	Total Elements	No. Nodes on Blade surface	Inflation Layers
A	161065	100317	261382	200	20
B	242916	231660	474576	500	30
C	583015	278645	861660	900	40
D	1169414	415150	1584564	1300	50

Richardson's Extrapolation (equations 13-15) is applied for the spatial discretisation study of the full turbine. The analysis is performed for *TSR* = 1. Results for the averaged torque coefficient, $\bar{C}_Q$, per cycle for each of the meshes are presented in Table 7.

Table 7
$\overline{C_Q}$ results for a series of four increasingly refined meshes (*TSR* = 1).

Mesh	$\overline{C_Q}$	$\%\overline{C_Q}$
A	0.007	84.9
B	0.036	23.5

C	0.046	0.05
D	0.047	-0.93
Richardson's extrapolation value		0.046

Fig. 10 presents the finalised averaged torque coefficient against the normalised mesh size for *TSR* = 1. Mesh C and D are both within 1 % of the final RE value. Due to the lower computational resource requirement of running simulations using Mesh C, this is chosen as the mesh for all following simulations.

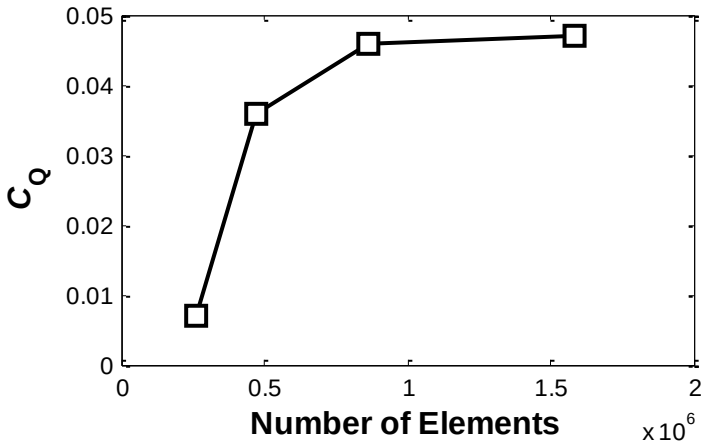

Fig. 10. Mesh convergence study results for full turbine CFD model (*TSR* = 1).

Temporal discretisation

A temporal discretisation study is carried out for the full turbine CFD model for *TSRs* of 1 and 2.5. The study focuses on establishing the optimum time step size and the determining the number of rotations required to achieve the convergence criterion for the average torque coefficient.

Table 8 and 9 present results for different time step increments based on the size of each degree increment per time step. To achieve the desired accuracy a time step increment equivalent to Δ 0.5° is selected for *TSR* ≤ 1.5. For *TSR* > 1.5 a time step increment equivalent to Δ 1° is selected based on the results presented in Table 9 for *TSR* = 2. A smaller time step is required at lower *TSR* due to complex flow phenomenon that occur at these low speeds relating to the dynamic stall of the turbine.

Table 8

$\bar{C}_Q$ results for a range of Δ°/step for *TSR* = 1.

Δ°/step	$\overline{C_Q}$
2°	0.033
1°	0.039
0.5°	0.045
0.25°	0.046

Table 9

$\bar{C}_Q$ results for a range of Δ°/step for *TSR* = 2.5.

Δ°/step	$\overline{C_Q}$
2°	0.1123
1°	0.1264
0.5°	0.1265

0.25º -

Fig. 11 presents the convergence history for a *TSR* = 1. Following 28 rotations a steady state solution has been achieved with a convergence factor of 0.05%. The rate of convergence is slower for higher TSRs, for example, a TSR of 2.5 reaches a convergence factor of 0.3% following 28 rotations.

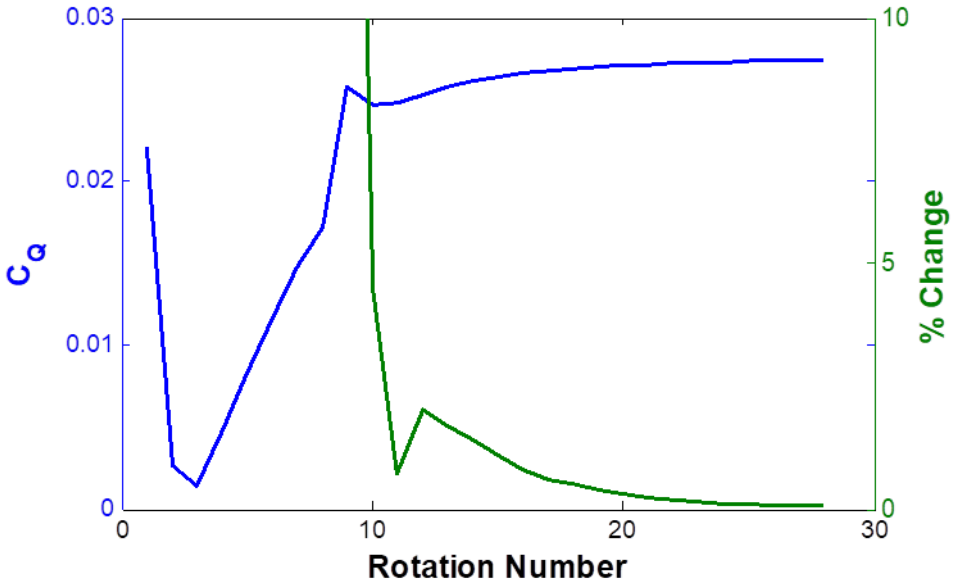

Fig. 11. Evolution of average torque coefficient as a function of number of turbine rotations leading to steady-state solutions (*TSR* = 1). Convergence factor (% change in $\bar{C}_Q$ from previous rotation) also indicated.

4-2. Lift and drag coefficients comparison

Computed values of C_L and C_D from the CFD analyses are compared to experimental data. The experimental study of Jacobs (1937) reports values of C_L and C_D for the NACA0015 profile for α between 0º and 24º and a wide range of *Re*. Sheldhal and Klimas (1981) performed experiments for a wide range of α between 0º and 180º over a narrow spread of *Re* (3.6×10^5, 5×10^5 and 6.7×10^5).

For direct comparison with available experimental data CFD results are computed for $Re = 8.8 \times 10^4$, 5×10^5 and 1.27×10^6, as shown in Fig. 13. In terms of C_L the CFD model provides an accurate prediction of the experimentally measured maximum value of C_L and the corresponding value of α for all three values of *Re*. The CFD model correctly predicts the onset of stall and is far more accurate than the panel method data (comparing Fig. 4 and Fig. 13 (a)). The model also correctly predicts the critical stall region following maximum C_L. The capability of the CFD model to compute the laminar to turbulent transition is critical for such accurate predictions of the complex relationship between C_L, α, and *Re*. There is a reduced amount of data available for the coefficient of drag, C_D, however, for the data available accurate predictions are achieved by the CFD model. Simulations exhibit a strong dependence of C_L and C_D on *Re* in the stall region. At low α (< 7°) and high α (> 27°) C_L and C_D do not exhibit a significant dependence on *Re*. This is consistent with experimental measurement; Sheldahl and Klimas (1981) report that C_L and C_D are independent of *Re* for $\alpha > 30°$.

Fig. 14 shows the pressure coefficient, C_p, distribution variation along the chord length of upper and lower surfaces of the hydrofoil profile. The CFD results are validated against published experimental results (Miller, 2008) for a constant *Re* of 2.3×10^5 and α values of 5º, 10º and 15º. The CFD model provides an accurate prediction of the experimental data, further validating the modelling approach.

Discrepancies are observed between the CFD and experimental data for angles of attack in the post-stall region due to the unsteadiness of the flow. The lift and drag coefficients fluctuate and the CFD results presented in Fig. 13 are the mean of these fluctuations. These discrepancies are also evident in the results presented in Fig. 14. (c). For a larger angle of attack, α = 15º, there is an increased error in the model predictions, which can be attributed to the unsteadiness of the flow.

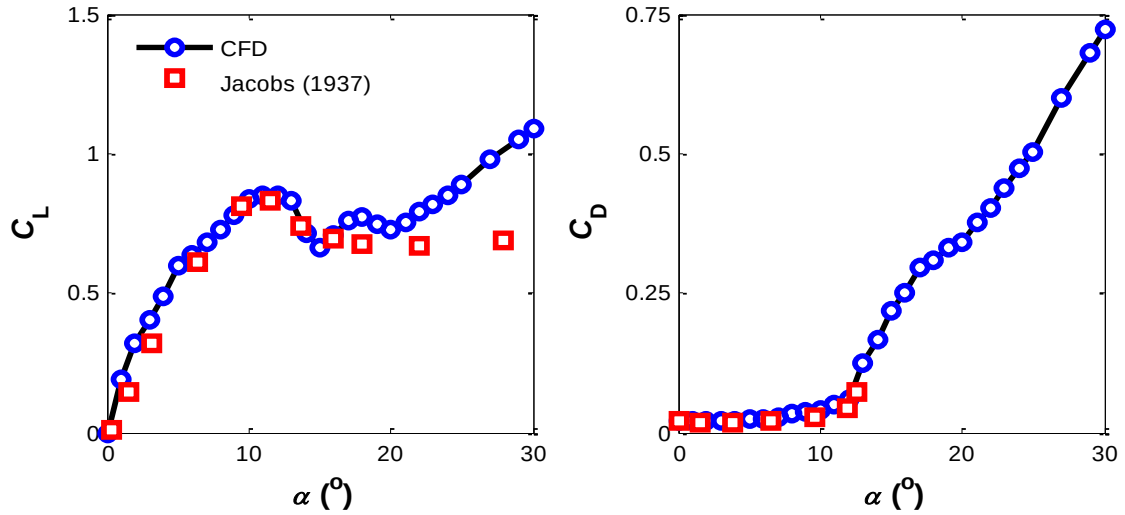

(a) $Re = 8.4 \times 10^4$

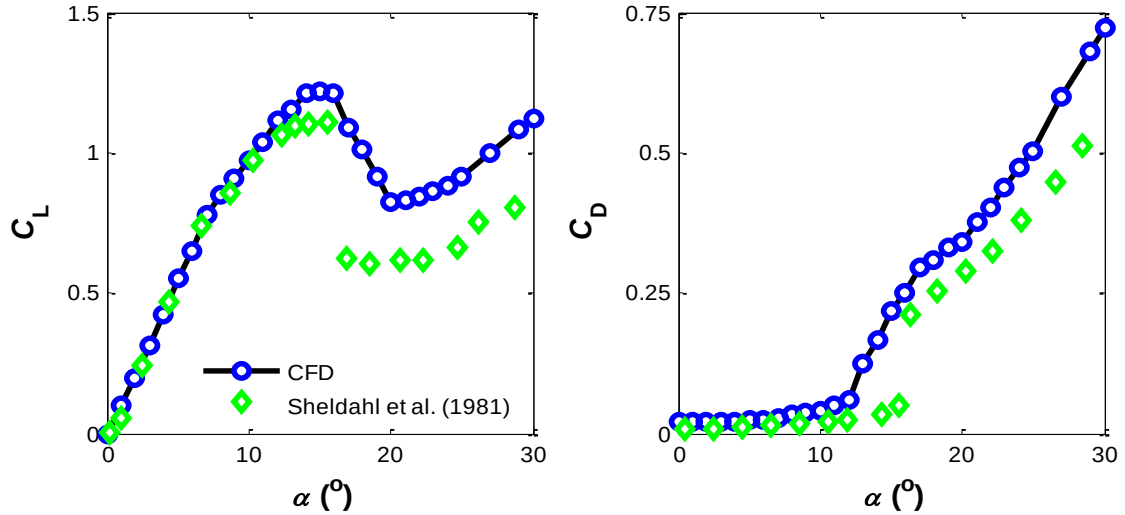

(b) $Re = 5 \times 10^5$

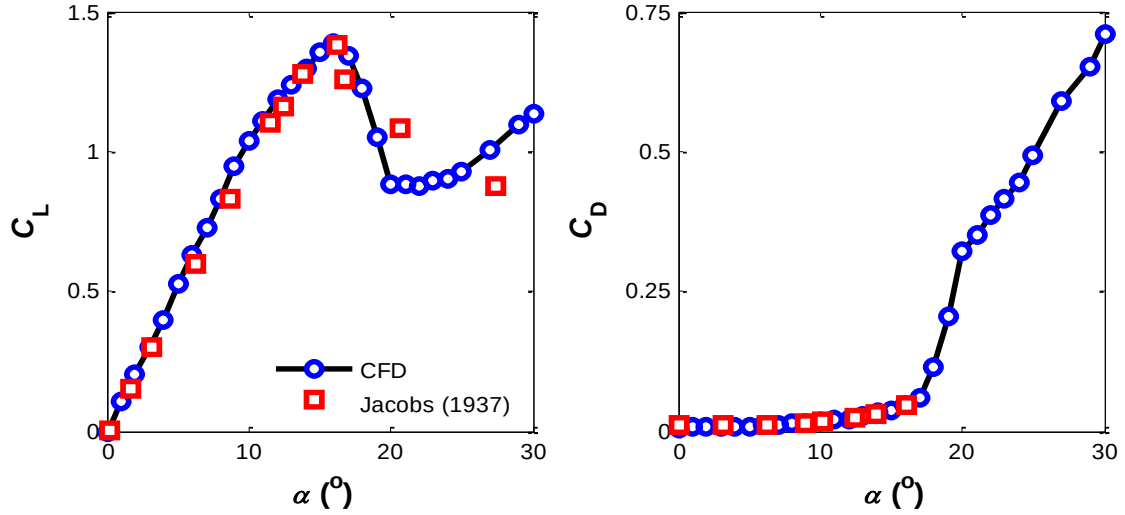

(c) $Re = 1.27 \times 10^6$

Fig. 12. CFD computed C_L and C_D for NACA0015 hydrofoil for a range of α. Results are compared to available experimental data for three values of Re: (a) 8.4×10^4; (b) 5×10^5; (c) 1.27×10^6.

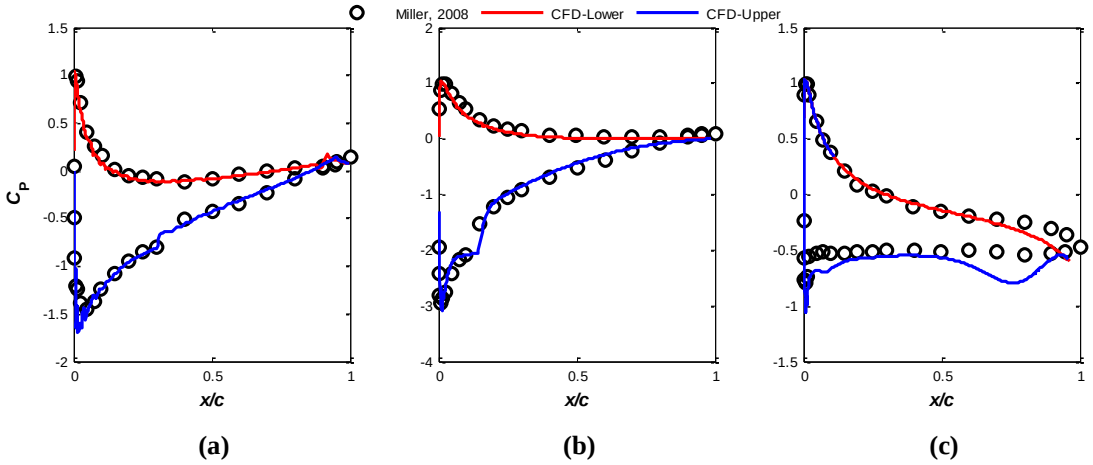

Fig. 13. CFD computed pressure coefficient as a function of position on the lower and upper hydrofoil surfaces for three values of α: (a) 5°; (b) 10°; (c) 15°. Re = 2.3 x 10^5 for all cases. Results are compared to published experimental data.

As mentioned in Section 3-1, a constant steady-state C_L or C_D is not achieved for α in the stall and post-stall region, due to the unsteady nature of the flow under these conditions. This is reflected in the results presented in Fig. 14 for $Re = 5 \times 10^5$. For $\alpha = 5^o$ the flow is steady and this is reflected in the constant values of C_L and C_D achieved. As α increases, the magnitude of the fluctuations of C_L and C_D increases. The time period of the fluctuations also increases with increasing angle of attack.

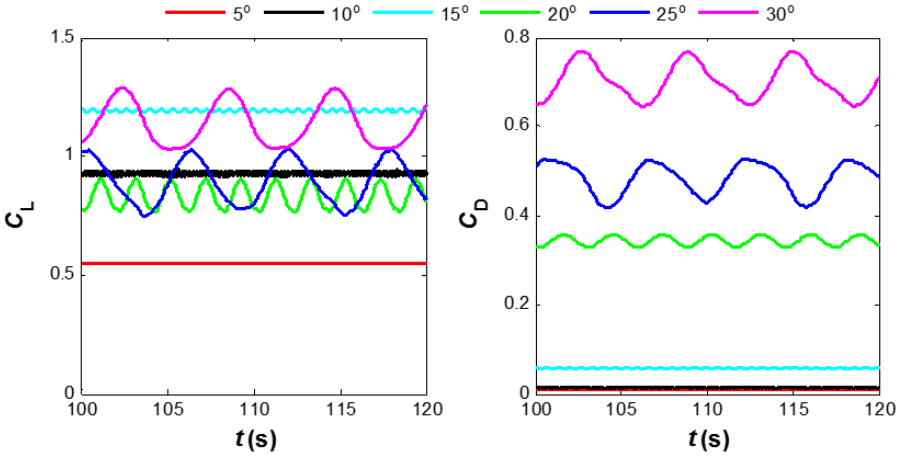

Fig. 14. Variation of lift and drag coefficients as a function of time for different angles of attack, once a periodic nature has been observed.

The following images detail some of the flow phenomena experienced by the hydrofoil at different angles of attack. Fig. 15 is a velocity streamline contour and streamline plot for $\alpha = 2^o$, $Re = 5 \times 10^5$. At this low angle of attack, there is very little to no flow separation. This highlights the rationale behind the high level of accuracy at low angles of attack between the CFD data, panel method data and experimental results comparisons shown in Fig. 12.

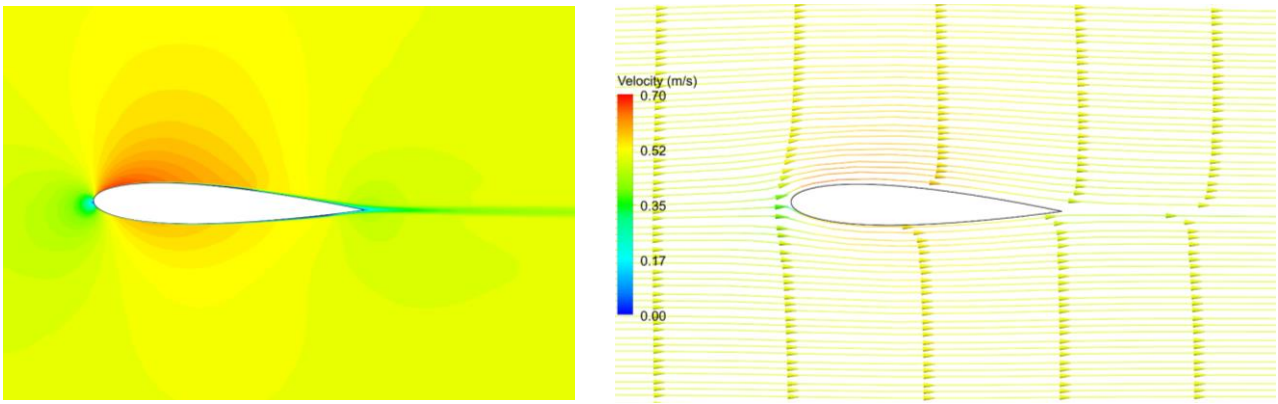

Fig. 15. Plot of velocity contours and streamlines for $\alpha = 2^o$ ($Re = 5 \times 10^5$).

Fig. 16 is a velocity contour and streamline plot for α = 15º, Re= 5 × 10^5. In the velocity contour plot, at the highlighted upper surface of the leading edge, the laminar separation bubble is beginning to form. This demonstrates the beginning of the onset of stall and is also highlighted in the results presented in Fig. 13 (b), where the lift coefficient drops significantly for the angles of attack slightly greater than 15º.

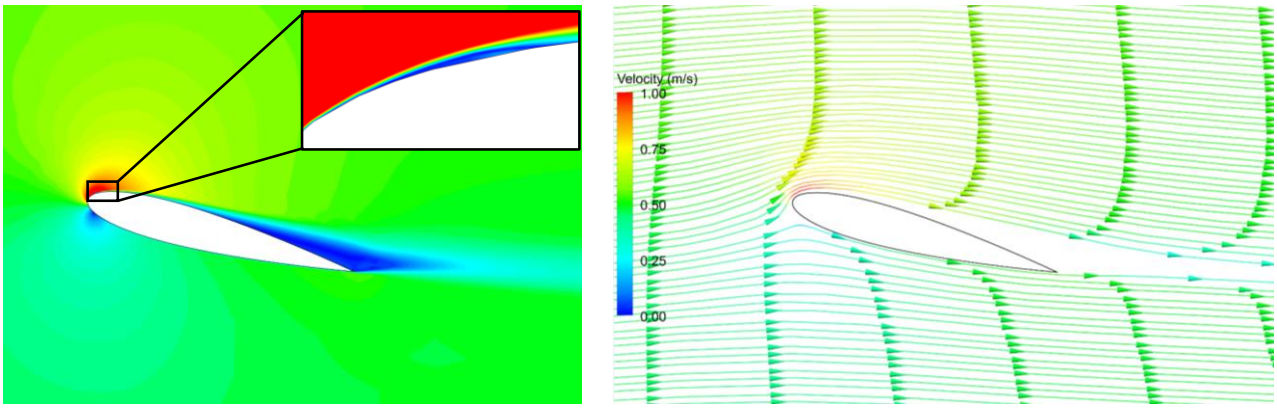

Fig. 16. Plot of velocity contours and streamlines for α = 15º (Re= 5 × 10^5), highlighted the beginning of the onset of stall.

Fig 17 shows the velocity contours and streamlines for α = 30º, Re= 5 × 10^5. At this angle of attack, the hydrofoil is in deep stall and the nature of the flow is highly unsteady, as is shown in Fig. 14. This is also reflected in the difference between the two sets of plots presented. In Fig. 17 (a), at time = 106.5 s, the hydrofoil experiences an instantaneous lift coefficient of 1.03 while in Fig. 17 (b), at time = 108.5 s, the instantaneous lift coefficient is 1.21. As evident in Fig. 17 (a) the recirculating flow contributes to reducing the overall lift coefficient on the hydrofoil, while when the flow remains detached, as shown in Fig. 17 (b), a greater maximum lift coefficient is achieved. These results also demonstrate the capability of the SST-T model to simulate flow separation and reattachment at high values of α.

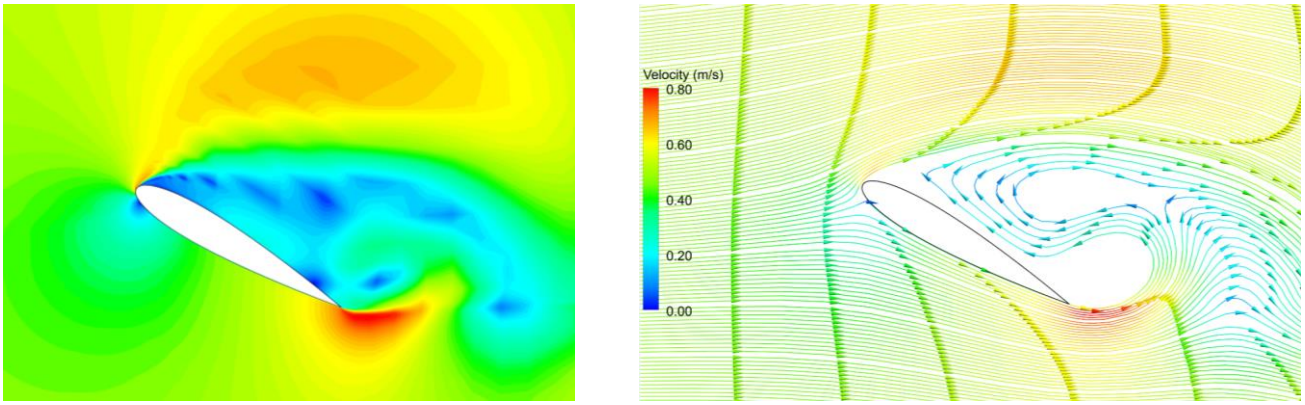

(a)

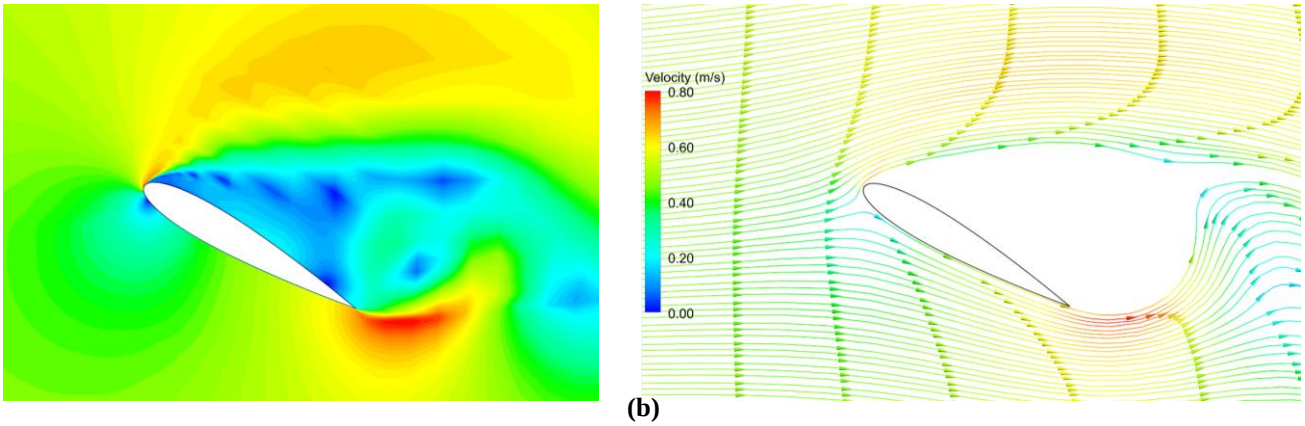

(b)

Fig. 17. Plots of velocity contours and streamlines for α = 30º (Re= 5 × 10^5) (a) Minimum lift (time = 106.5 s) and (b) Maximum lift (time = 108.5 s).

4-3. Turbine analysis

4-3.1. Straight-bladed vertical-axis turbine analysis

A comprehensive data-set for the dependence of C_L and C_D on *Re*, shown in Fig. 18, is generated using the validated SST-T CFD modelling approach. Simulations were performed for a range of α from 0° to 30° and a range of *Re* from 8.4×10^4 to 2×10^6 with the critical stall region being identified for each case. The results exhibit the strong dependence of C_L and C_D on *Re* in this stall region. At low α (< 7°) and high α (> 27°) C_L and C_D do not exhibit a significant dependence on *Re*. This is consistent with experimental measurement; (Sheldahl and Klimas, 1981) report that C_L and C_D are independent of *Re* for $\alpha > 30°$.

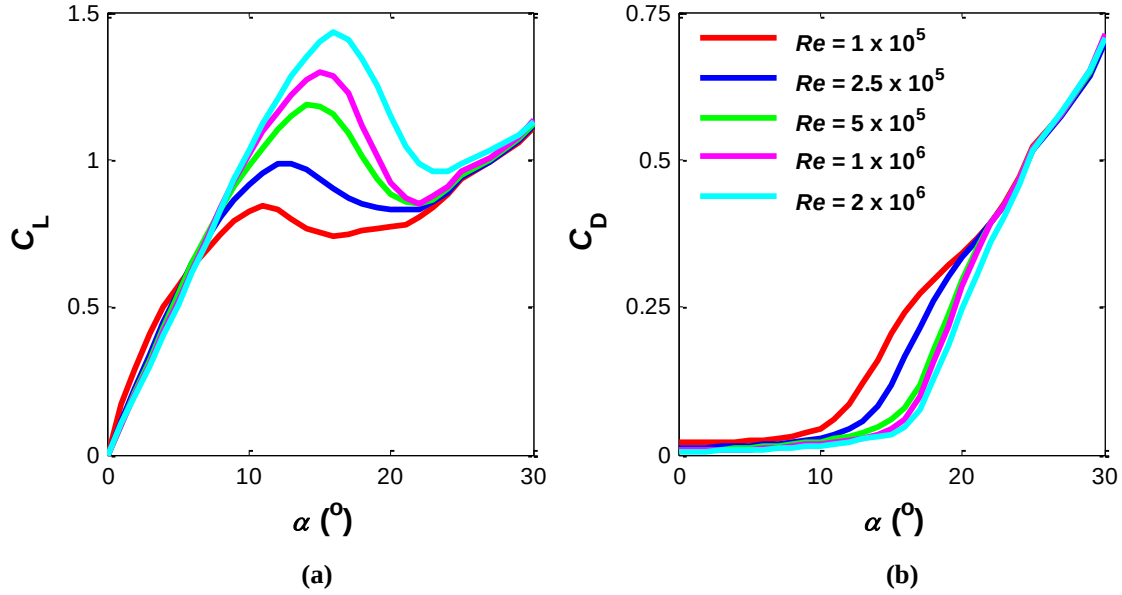

Fig. 18. CFD data-set showing (a) C_L and (b) C_D as a function of angle of attack (α) for a range of Reynolds numbers (*Re*).

In a companion study (Heavey et al., 2018), written by the authors of this paper, a blade element momentum code was developed to analyse the power performance of the novel vertical-axis turbine (Fig. 2.). In that study panel method dataset was used as input into the BEM code. For the results presented in this section, the panel method dataset is replaced by the CFD dataset shown in Fig. 15. This BEM code is in the form of a double multiple streamtube model which incorporates a dynamic stall model, finite aspect ratio effects, flow expansion and a fluid velocity profile. The turbine is divided into separate upstream and downstream halves. The fluid flow velocities and forces are initially determined for the upstream half of the turbine. The flow velocities calculated from the upstream half of the turbine are subsequently used as input into the calculations for the downstream half of the turbine. The model steps through both blade position and blade height to determine the instantaneous torque on each blade elements which is averaged over a full rotation to calculate the average power.

The power performance of this turbine is studied by establishing C_{power} over a range of *TSR*. C_{power} and *TSR* are dimensionless parameters that readily facilitate comparison of the hydrodynamic performance of turbines designs under a range of flow conditions.

Fig. 19 presents a comparison between three sets of model results against experimental data (McLaren, 2011) for a straight bladed vertical-axis turbine (Table 1). While the experimental tests were carried out with a blockage ratio of 3%, testing protocols published by (Bahaj, Blunden and Anwar, 2008) state that experimental power curves results for tidal current turbines require a correction coefficient when the blockage ratio is above 5%. Therefore the experimental results could be treated as freestream conditions.

Two sets of BEM results are included; one which incorporates the panel method data-set (Sheldahl and Klimas, 1981) and the other which incorporates the newly developed CFD data-set. A double linear interpolation, for both α and *Re*, is carried out within the code. Also included in Fig. 19 are results for the full two-dimensional CFD studies, described in Section 3-2. Results are compared to wind tunnel experimental data for an identical straight bladed turbine (Table 2). Experimental operational *Re* values are identical to model values and the low experimental Mach numbers (< 0.3) justify the model assumption of fluid incompressibility.

All the results follow the expected trend of turbine power curves, with poor power performance at low TSRs followed by a sharp increase to an optimum TSR for maximum power performance, before a gradual decrease in power performance at higher TSRs. Root-mean-squares errors (RMSEs) between experimental data and model predictions shown in Table 10 suggest that both the CFD-based BEM model and the full CFD turbine model provide a significantly higher level of accuracy that the PM-based BEM model. The best agreement is obtained between experimental and CFD-based BEM results. For $1.5 > TSR > 2.25$, the peak power range, the model predictions are within the experimentally observed range.

A very similar level of accuracy to the CFD-based BEM is achieved by the full CFD model, with both models predicting the maximum C_{Power} of 0.35 at a *TSR* of 2 and both sets of results following similar trends at lower and higher *TSRs*. The advantage of the CFD-based BEM model over the full CFD model lies in the dramatically decreased computational cost. The once-off computational cost of generating a CFD-based hydrofoil data set for the required range of alpha and Re is 18600 CPU hours. Once generated, a turbine design can be accurately simulated in under 30 seconds on a single CPU. In contrast, an analysis of a single turbine design using the full CFD modelling approach requires 32640 CPU hours. The CFD-based BEM method, therefore, offers a computationally viable approach for design and optimisation of vertical axis turbines with significant improvements in predictions over the traditional panel method based BEM.

Table 10
Goodness of fit of various turbine models with experimental test data (McLaren, 2011).

Comparison	RMSE
CFD-based BEM	0.0033
Full CFD	0.0040
PM-based BEM	0.0070

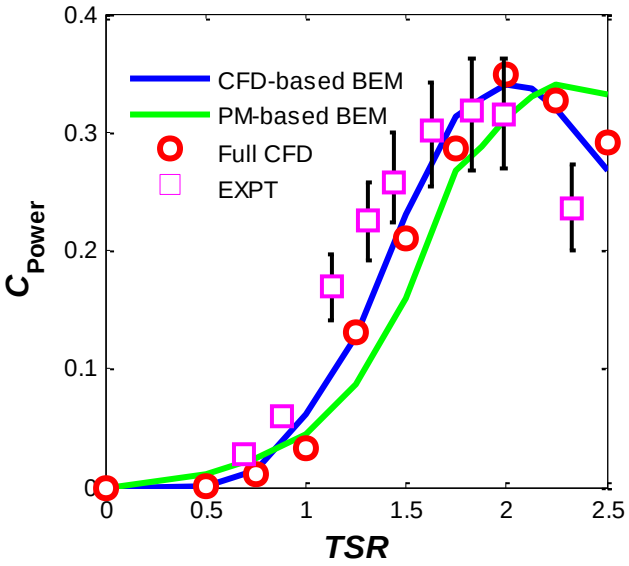

Fig. 19. Comparison between CFD-based BEM model, Panel Method- (PM-) based BEM model and full CFD model predictions with published experimental results for a straight-bladed vertical axis turbine (Table 1). The accuracy (RMSE) of each of the model predictions is listed in Table 10.

Table 11
Computational cost of both methodologies.

Method	Time (hrs)	No. Processors	Total CPU (hrs)
CFD-generated hydrofoil data-set	775	24	18600
Single full CFD simulation of VATT	680	48	32640

Fig. 20 shows the variation of vorticity with different blade orientations for a straight-bladed vertical-axis turbine operating at its optimum TSR of 2. It can be noted that the magnitude of the flow field vorticity around the hydrofoil is low for

azimuthal angles of 0-90°. There is a significant increase in the vorticity as the blade reaches an azimuthal angle of 120°, followed by the shedding of vortices seen for azimuthal angles of 150-210°.

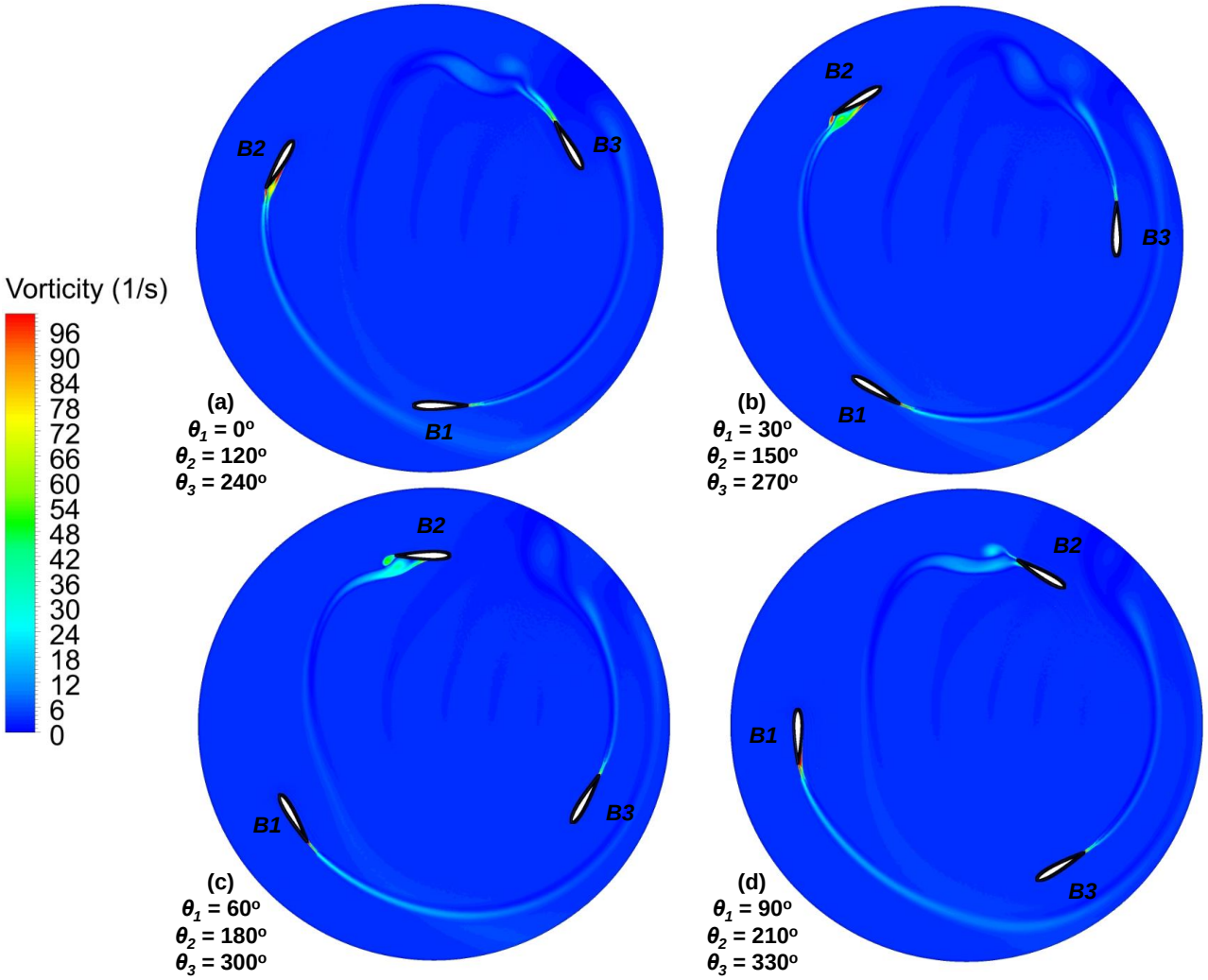

Fig. 20. Magnitude of the flow vorticity for a straight-bladed vertical-axis turbine (Table 1) operating at TSR = 2 for a number of varying blade orientations (a)- (d) with the freestream flow from left to right in each case.

4-3.2. Novel vertical-axis turbine analysis

Finally, the CFD-based BEM approach is used to analyse the novel turbine geometry shown in Fig. 2. The turbine parameters and fluid conditions are listed in Table 12. Fig. 21 shows the power performance prediction curves of this turbine when implementing the two sets of hydrodynamic coefficients; CFD-based and the traditional panel method dataset. The maximum power coefficient for each result is the same; however, the CFD-based dataset predicts that the maximum power coefficient will occur at a *TSR* of 4.5 compared to 5.5 for the panel method data-set.

Table 12
Key parameters and turbine features for BEM rotor simulations.

Fluid conditions: Seawater at 5 °C	
Density	1025 kg m^{-3}
Viscosity	0.00162 Ns m^{-2}
Velocity	2 m s^{-1}
Turbine Features:	
Chord	0.15 m
Number of blades	3
Diameter	3 m

Blade profile	NACA0015

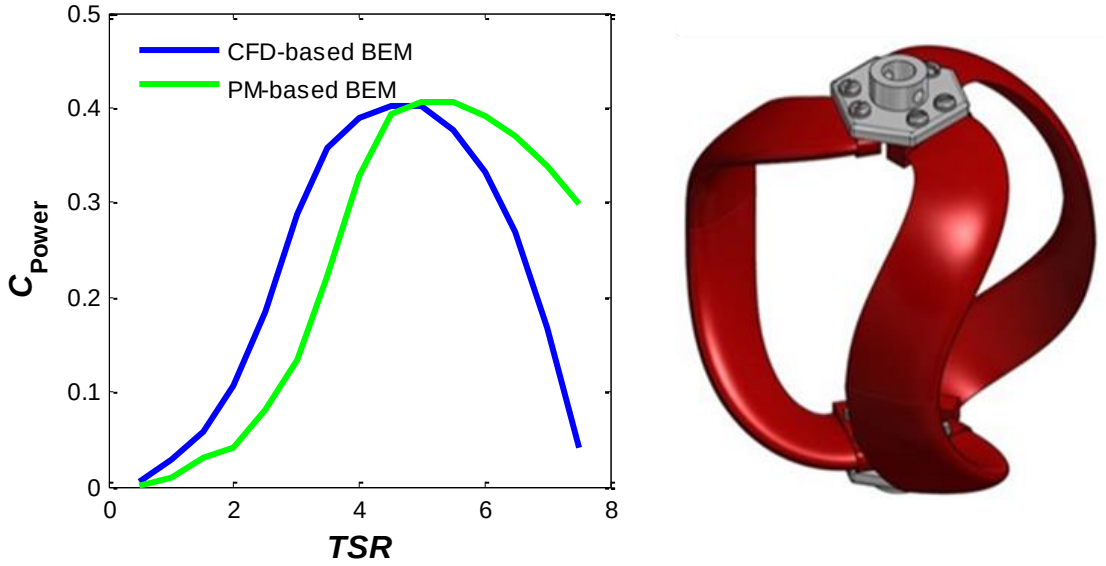

Fig. 21. Variation of power coefficient with *TSR* for the novel vertical axis turbine design.

The variation of the instantaneous torque with azimuthal angle for the novel turbine design is shown in Fig. 22. Three different TSR are examined and results from the BEM code incorporating both the panel method data and the newly developed CFD-based dataset are compared. The CFD-based BEM model has proven to be the more accurate method for analysing alternative turbine designs (Fig. 19). The instantaneous torque loads presented are directly proportional to the structural loads experienced by the turbine, so a failure to accurately predict these loads could have significant effects not only on the power performance but also the structural integrity and safety of the turbine. We can see that the most significant error occurs in Fig.2 (a) (*TSR* = 2), which coincides with the operational conditions when the turbine is experiencing its largest range of α and *Re*.

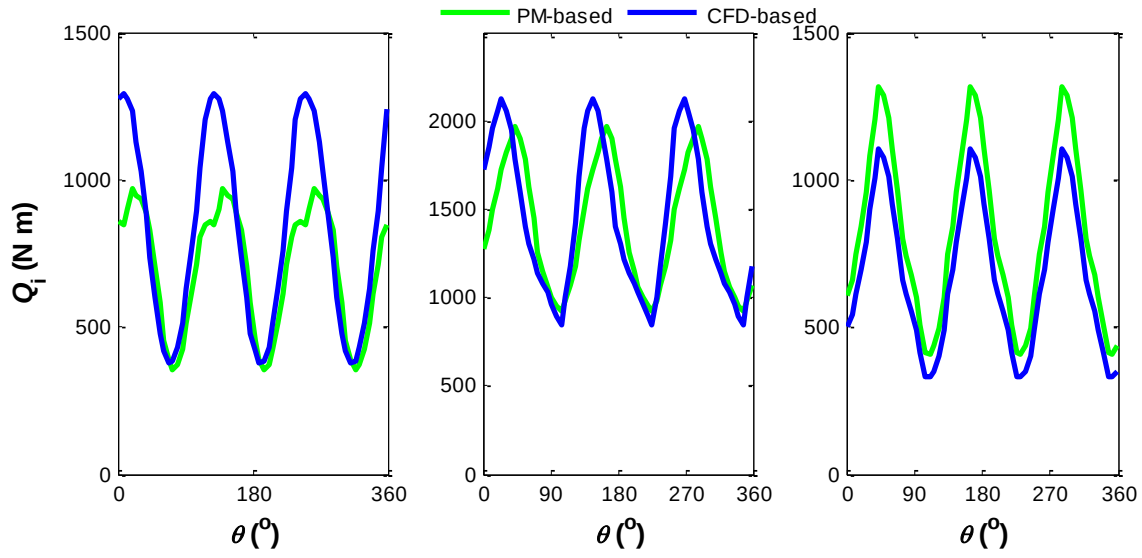

(a) *TSR* = 2 **(b) *TSR* = 4** **(c) *TSR* = 6**

Fig. 22. Variation of instantaneous torque with blade position for the novel vertical-axis turbine design. Comparison between CFD-based BEM and PM-based BEM results for (a) TSR = 2, (b) TSR = 4 and (c) TSR = 6.

5. Conclusions

An improved method is presented for hydrodynamic assessment and preliminary design of tidal turbines based on CFD RANS analysis of a hydrofoil for a range of angles of attack and Reynolds numbers, combined with a BEM model. The

input of accurate lift and drag coefficient data-set is critical for BEM modelling of vertical axis turbines, particularly for spiral and helical blade turbines (Cheng et al., 2017; Talukdar et al., 2017; Walsh et al., 2015). Such complex turbine designs experience significant variations of angles of attack and Reynolds numbers under standard operational conditions.

Using the example of a NACA0015 hydrofoil this study demonstrates that a SST transitional turbulence CFD modelling approach can be used to accurately determine lift and drag coefficients across for wide range of Reynolds numbers and angles of attack required for vertical axis turbine analysis. Previous SST-T analyses of aerofoils have considered only a limited range of Reynolds number and angle of attack. The ability of the modelling approach to capture flow transition from laminar to turbulent is essential in generating accurate data, particularly in the stall region, as shown in Figure 13. In contrast, the widely used panel method (Sheldahl and Klimas, 1981) does not accurately predict the relationship between the coefficient of lift and angle of attack for low Reynolds numbers, as shown in Figure 4.

The results presented in this paper highlight that RANS modelling offers a computationally viable means of determining lift and drag coefficients for a range of angles of attack and Reynolds numbers. At angles of attack in the deep stall region ($\alpha > 20^{o}$) the accuracy of the model is reduced due to the highly unsteady behaviour of the flow. Turbulence in its nature is three-dimensional so future studies will examine three-dimensional RANS modelling of a finite length hydrofoil as implemented in the experimental study. By investigating these three-dimensional flow fields possible reasons for discrepancies between the two-dimensional numerical results and experimental data may be identified.

It is demonstrated that BEM models provide improved predictions of vertical axis turbine performance when CFD generated lift and drag coefficients are used as input, rather than coefficients generated by the widely used panel-method. We demonstrate that a BEM model which implements a CFD generated hydrofoil dataset achieves a similar level of accuracy to a full CFD turbine model but at a significantly lower computational cost. The computational efficiency of RANS CFD analysis of hydrofoils combined with the BEM modelling of turbine performance provides an efficient design platform for the development of complex non-straight bladed next-generation vertical axis turbine designs such as those proposed by (McGuire, 2014; Preen and Bull, 2015; Shires, 2013)).

Acknowledgements

This research is funded by Science Foundation Ireland under Grant Number SFI/12/RC/2302 and also by Bernard McGuire and Bobby Willis of Bri Toinne Teoranta.

The authors wish to acknowledge the DJEI/DES/SFI/HEA Irish Centre for High-End Computing (ICHEC) for the provision of computational facilities and support.

Nomenclature

$\vec{a}$	force vector	R	radius [m]
A	area [m^2]	r	refinement ratio
BEM	blade element momentum	R^*	convergence constant
c	chord length [m]	RANS	Reynolds averaged Navier-Stokes
C_{D}	drag coefficient	Re	Reynolds number
C_{L}	lift coefficient	$Re_{\theta,\mathrm{c}}$	critical Reynolds number
C_{p}	pressure coefficient	$Re_{\theta,\mathrm{t}}$	transition Reynolds number
C_{power}	power coefficient	RMSE	root mean square error
C_Q	instantaneous torque coefficient	SST-T	shear stress transport transition
$\bar{C}_{\mathrm{Q}}$	average torque coefficient	TSR	tip speed ratio
CPU	computer processing unit	u	flow velocity parallel to face
D	diameter [m]	$U_{i,T}$	turbine inlet velocity
DES	detached eddy simulation	$U_{i,H}$	hydrofoil inlet velocity
DMST	double multiple streamtube	U_∞	freestream velocity
DNS	direct numerical simulation	V^*	frictional velocity
$\vec{F}_a$	total force component [N]	VAT	vertical axis turbine

$\vec{F}_p$	pressure force component [N]	VATT	vertical axis tidal turbine
$\vec{F}_v$	viscous force component [N]	y	distance to the nearest wall [m]
HATT	horizontal axis tidal turbine	$y+$	non dimensional wall distance
HOT	higher order terms	α	angle of attack [deg]
k	turbulent kinetic energy [m^2 s^{-2}]	γ	Intermittency
L	lift force [N]	ε	turbulence dissipation rate [m^2 s^{-3}]
LES	large eddy simulation	θ	azimuthal angle [deg]
LSB	laminar separation bubble	μ	dynamic viscosity [N s/m^2]
Ma	Mach number	ρ	density [kg m^{-3}]
N	number of elements	τ_w	wall shear stress [Pa]
P	power [kW]	ω	specific turbulence dissipation rate [s^{-1}]
p	pressure [Pa]	ω_{rot}	rotational velocity [rad s^{-1}]
PM	panel method	υ	local kinematic viscosity [m^2 s^{-1}]
Q	torque [N m]		

References

Almohammadi, K.M., Ingham, D.B., Ma, L., Pourkashan, M., 2013. Computational fluid dynamics (CFD) mesh independency techniques for a straight blade vertical axis wind turbine. Energy 58, 483–493. https://doi.org/10.1016/j.energy.2013.06.012

ANSYS, 2013. ANSYS Fluent Theory Guide. Canonsburg, Pennsylvania. https://doi.org/10.1016/0140-3664(87)90311-2

Azeez, A., Paul, J., 2014. CFD Analysis of NACA 63-018 Airfoil at Different Reynolds-Number. Int. J. Eng. Trends Technol. 12, 258–264.

Battisti, L., Brighenti, A., Benini, E., Castelli, M.R., 2016. Analysis of Different Blade Architectures on small VAWT Performance. J. Phys. Conf. Ser. 753, 062009. https://doi.org/10.1088/1742-6596/753/6/062009

Chen, J., Yang, H.X., Liu, C.P., Lau, C.H., Lo, M., 2013. A novel vertical axis water turbine for power generation from water pipelines. Energy 54, 184–193. https://doi.org/10.1016/j.energy.2013.01.064

Cheng, Q., Liu, X., Ji, H.S., Kim, K.C., Yang, B., 2017. Aerodynamic Analysis of a Helical Vertical Axis Wind Turbine. Energies 10, 575. https://doi.org/10.3390/en10040575

Counsil, J.N.N., Goni Boulama, K., 2013. Low-Reynolds-Number Aerodynamic Performances of the NACA 0012 and Selig–Donovan 7003 Airfoils. J. Aircr. 50, 204–216. https://doi.org/10.2514/1.C031856

Counsil, J.N.N., Goni Boulama, K., 2012. Validating the URANS shear stress transport γ −Reθ model for low-Reynolds-number external aerodynamics. Int. J. Numer. Methods Fluids 69, 1411–1432. https://doi.org/10.1002/fld.2651

Dash, A., 2016. CFD Analysis ofWind Turbine Airfoil at Various Angles of Attack. IOSR J. Mech. Civ. Eng. 13, 18–24. https://doi.org/10.9790/1684-1304021824

Douvi, E., Tsavalos, A., Margaris, D., 2012. Evaluation of the turbulence models for the simulation of the flow over a National Advisory Committee for Aeronautics (NACA) 0012 airfoil. J. Mech. Eng. Res. 4, 100–111. https://doi.org/10.5897/JMER11.074

Eppler, R., 1978. Turbulent airfoils for general aviation. J. Aircr. 15, 93–99. https://doi.org/10.2514/3.58320

Genç, M.S., 2010. Numerical simulation of flow over a thin aerofoil at a high Reynolds number using a transition model. Proc. Inst. Mech. Eng. Part C J. Mech. Eng. Sci. 224, 2155–2164. https://doi.org/10.1243/09544062JMES2121

Goundar, J.N., Ahmed, M.R., 2013. Design of a horizontal axis tidal current turbine. Appl. Energy 111, 161–174. https://doi.org/10.1016/j.apenergy.2013.04.064

Heavey, S., Leen, S., McGarry, P., 2018. Hydrodynamic design and analysis of a novel vertical axis turbine. Int. J. Offshore Polar Eng. IN PRESS

Hill, N., Dominy, R., Ingram, G., Dominy, J., 2009. Darrieus turbines: the physics of self-starting. Proc. Inst. Mech. Eng.

Part A J. Power Energy 223, 21–29. https://doi.org/10.1243/09576509JPE615

Jacobs, E.N., Sherman, A., 1937. Airfoil section characteristics as affected by variations of the Reynolds number. NACA Rep. 586. https://doi.org/19930091662

Langtry, R.B., Menter, F.R., Likki, S.R., Suzen, Y.B., Huang, P.G., Völker, S., 2006. A Correlation-Based Transition Model Using Local Variables—Part II: Test Cases and Industrial Applications. J. Turbomach. 128, 423. https://doi.org/10.1115/1.2184353

Lewis, M., Neill, S.P., Robins, P.E., Hashemi, M.R., 2015. Resource assessment for future generations of tidal-stream energy arrays. Energy 83, 403–415. https://doi.org/10.1016/j.energy.2015.02.038

Li, C., Zhu, S., Xu, Y., Xiao, Y., 2013. 2.5D large eddy simulation of vertical axis wind turbine in consideration of high angle of attack flow. Renew. Energy (UK) 51, 317–30.

Maître, T., Amet, E., Pellone, C., 2013. Modeling of the flow in a Darrieus water turbine: Wall grid refinement analysis and comparison with experiments. Renew. Energy 51, 497–512. https://doi.org/10.1016/j.renene.2012.09.030

McGuire, B., 2014. Turbine and a rotor for a turbine. US 8690541 B2.

McLaren, K., 2011. A numerical and experimental study of unsteady loading of high solidity vertical axis wind turbines. McMaster University.

McNaughton, J., Billard, F., Revell, a., 2014. Turbulence modelling of low Reynolds number flow effects around a vertical axis turbine at a range of tip-speed ratios. J. Fluids Struct. 47, 124–138. https://doi.org/10.1016/j.jfluidstructs.2013.12.014

Menter, F.R., 1994. Two-equation eddy-viscosity turbulence models for engineering applications. AIAA J. 32, 1598–1605. https://doi.org/10.2514/3.12149

Menter, F.R., Langtry, R.B., Likki, S.R., Suzen, Y.B., Huang, P.G., Völker, S., 2006. A Correlation-Based Transition Model Using Local Variables—Part I: Model Formulation. J. Turbomach. 128, 413. https://doi.org/10.1115/1.2184352

Miller, S.D., 2008. Lift, drag and moment of a NACA 0015 airfoil. Ohio State University.

Preen, R.J., Bull, L., 2015. Toward the Coevolution of Novel Vertical-Axis Wind Turbines. IEEE Trans. Evol. Comput. 19, 284–294. https://doi.org/10.1109/TEVC.2014.2316199

Roache, P.J., 1997. Quantification of uncertainty in computational fluid dynamics. Annu. Rev. Fluid Mech. 19, 123–160.

Sagmo, K., Bartl, J., Saetran, L., 2016. Numerical simulations of the NREL S826 airfoil. J. Phys. Conf. Ser. 753, 1–9. https://doi.org/10.1088/1742-6596/753/8/082036

Şahin, İ., Acir, A., 2015. Numerical and Experimental Investigations of Lift and Drag Performances of NACA 0015 Wind Turbine Airfoil. Int. J. Mater. Mech. Manuf. 3, 22–25. https://doi.org/10.7763/IJMMM.2015.V3.159

Shan, H., Jiang, L., Liu, C., 2005. Direct numerical simulation of flow separation around a NACA 0012 airfoil. Comput. Fluids 34, 1096–1114. https://doi.org/10.1016/j.compfluid.2004.09.003

Sheldahl, R.E., Klimas, P.C., 1981. Aerodynamic characteristics of seven symmetrical airfoil sections through 180-degree angle of attack for use in aerodynamic analysis of vertical axis wind turbines SAND80-211, 118. https://doi.org/10.2172/6548367

Shires, A., 2013. Development and evaluation of an aerodynamic model for a novel vertical axis wind turbine concept. Energies 6, 2501–2520. https://doi.org/10.3390/en6052501

Stergiannis, N., Lacor, C., Beeck, J. V, Donnelly, R., 2016. CFD modelling approaches against single wind turbine wake measurements using RANS. J. Phys. Conf. Ser. 753, 032062. https://doi.org/10.1088/1742-6596/753/3/032062

Svorcan, J., Stupar, S., Komarov, D., Peković, O., Kostić, I., 2013. Aerodynamic design and analysis of a small-scale vertical axis wind turbine. J. Mech. Sci. Technol. 27, 2367–2373. https://doi.org/10.1007/s12206-013-0621-x

Talukdar, P.K., Kumar, S., Kulkarni, V., Das, A.K., Saha, U.K., 2017. On site testing of a zero head vertical axis helical turbine, in: Proceedings of the ASME 2015 Gas Turbine India Conference. pp. 1–6.

Walsh, G.P., Keough, R., Mullaley, V., Sinclair, H., Hinchey, M.J., 2015. Cross-flow helical turbine for energy production in reversing tidal and ocean currents. 2014 Ocean. - St. John's, Ocean. 2014 2–7. https://doi.org/10.1109/OCEANS.2014.7003267

Wang, S., Ingham, D.B., Ma, L., Pourkashanian, M., Tao, Z., 2010. Numerical investigations on dynamic stall of low

Reynolds number flow around oscillating airfoils. Comput. Fluids 39, 1529–1541. https://doi.org/10.1016/j.compfluid.2010.05.004